Energy Storage Materials 13 (2018) 112–118

Contents lists available at ScienceDirect

Energy Storage Materials

journal homepage: www.elsevier.com/locate/ensm

Monodisperse and homogeneous SiO_x/C microspheres: A promising high-capacity and durable anode material for lithium-ion batteries

Zhenhui Liu, Doudou Guan, Qiang Yu, Lin Xu, Zechao Zhuang, Ting Zhu, Dongyuan Zhao, Liang Zhou*, Liqiang Mai*

State Key Laboratory of Advanced Technology for Materials Synthesis and Processing, Wuhan University of Technology, Wuhan 430070, PR China

ARTICLE INFO

Keywords:
Silicon oxide
Nanocomposite
Lithium storage
Anode
Full cell

ABSTRACT

Monodisperse SiO_x/C microspheres with tunable size (300–1000 nm) and well-controlled carbon content (~ 20–60 wt%) have been fabricated through a facile sol-gel method. The judicious selection of silicon and carbon precursors (vinyltriethoxysilane and resorcinol/formaldehyde) enables the formation of an homogeneous SiO_x/C (x = 1.63) composite, in which the SiO_x mainly exists as ultrafine nano-domains (< 2 nm). Benefiting from the unique structural features, the resultant SiO_x/C microspheres demonstrate high capacity and outstanding cyclability. Specifically, a reversible capacity of 999 mA h g^{-1} can be achieved at 100 mA g^{-1}, retaining 853 mA h g^{-1} after 150 cycles. At 500 mA g^{-1}, the SiO_x/C delivers a specific capacity of 689 mA h g^{-1} and maintains 91.0% of the capacity after 400 cycles. SiO_x/C//$LiFePO_4$ full cells are also assembled, leading to an energy density of ~ 372 W h kg^{-1} based on the total mass of active materials. This work sheds light on the rational design of high-performance SiO_x based anode materials for lithium-ion batteries.

1. Introduction

As a well-known energy storage device, lithium-ion batteries (LIBs) have been extensively applied in portable electronics because of their high energy density, long cycle life, and no memory effect [1–5]. However, the performance of current state-of-the-art LIBs cannot meet the increasing demand. Tremendous efforts have been dedicated to developing novel high-capacity electrode materials. As for the anode materials, silicon (Si) has attracted great interest as the prime alternative due to its high theoretical capacity (4200 mA h g^{-1}) and abundant reserves. However, two issues seriously hamper the practical application of Si: (1) remarkable volume change (> 400%) during cycling, which leads to poor cycling performance; (2) low conductivity, which limits the rate capability [6–8]. A number of strategies, such as fabricating nanostructured Si and Si-based composite materials, have been developed to tackle these issues [9–12]. Despite the encouraging advances have been achieved, the high manufacturing cost of nanostructured Si still remains unaffordable for practical applications.

Silica, also known as silicon dioxide (SiO_2), is the major constituent of sand. Although bulk SiO_2 shows little activity towards lithium, nanostructured SiO_2 has been demonstrated to be electrochemically active. For example, Gao et al. found that commercial SiO_2 nanoparticles (7 nm) exhibited a reversible capacity of ~ 400 mA h g^{-1} when reacting with lithium [13]. Yu et al. reported that carbon coated SiO_2 nanoparticles could deliver a discharge capacity of over 500 mA h g^{-1} with good cyclability [14]. Hollow porous SiO_2 nanocubes prepared by Yan et al. exhibited a high reversible capacity of 920 mA h g^{-1} [15]. Chang et al. reported that mechanically activated quartz (SiO_2) could deliver a reversible capacity of 800 mA h g^{-1} [16]. Silicon sub-oxides (SiO_x) have also been studied as a promising substitute for Si. Compared to Si, the SiO_x exhibits several advantages, such as lower cost, easier synthesis, and less volume expansion. In addition, the inert Li_2O and lithium silicates (Li_4SiO_4, $Li_2Si_2O_5$) generated in the initial lithiation process can buffer the volume variation and help to maintain the structural stability [17–19]. However, like elemental Si, the widespread application of SiO_x is limited by its low conductivity and large volume change. A series of SiO_x/C composites, such as hierarchical SiO_x/C [20], SiO_x/C dual-phase glass [21], SiO_x@C microspheres [22], and SiO_x@C nanorods [23], have been designed to improve the electrochemical performance. Although significant improvements have been achieved, the facile synthesis of SiO_x/C composites with tunable structure and excellent lithium storage performance remains a great challenge.

In this work, we report the facile sol-gel synthesis of monodisperse SiO_x/C microspheres with tunable size and well-controlled carbon content. With the homogeneous dispersion of SiO_x ultrafine nano-domains in an amorphous carbon matrix, the electronic conductivity of SiO_x can be significantly enhanced and the large volume variation can

* Corresponding authors.
E-mail addresses: liangzhou@whut.edu.cn (L. Zhou), mlq518@whut.edu.cn (L. Mai).

https://doi.org/10.1016/j.ensm.2018.01.004
Received 17 November 2017; Received in revised form 15 December 2017; Accepted 2 January 2018
Available online 04 January 2018

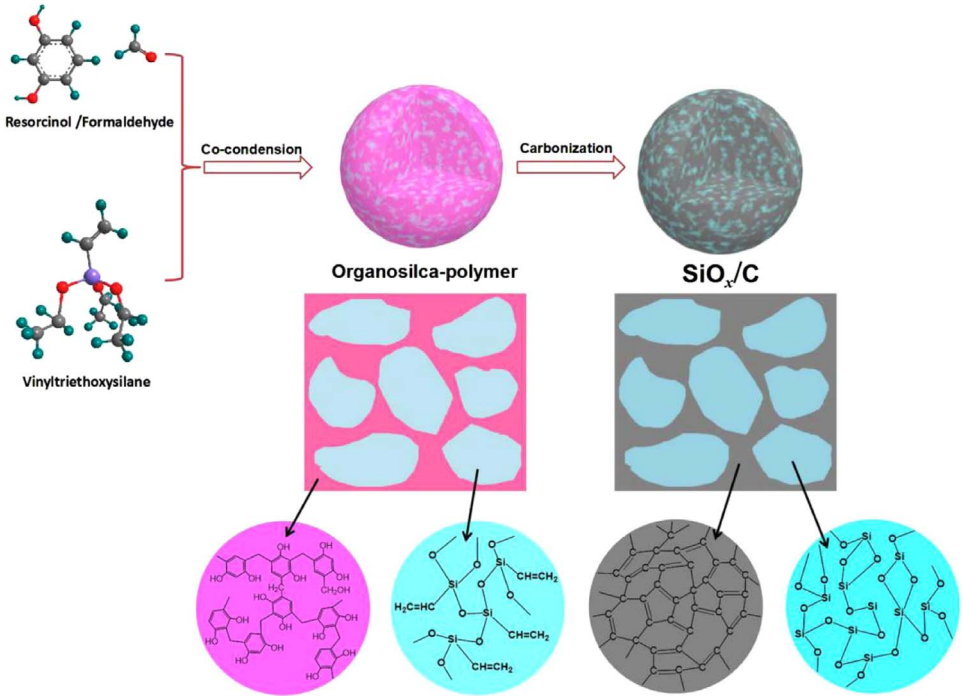

Fig. 1. Schematic illustration for the preparation of SiO_x/C microspheres. The synthesis relies on the simultaneous condensation of organosilica and RF.

be effectively buffered. The as-obtained SiO_x/C composite demonstrate high capacity and excellent cycling stability in lithium storage. A high reversible capacity of 999 mA h g^{-1} can be achieved at 100 mA g^{-1}, maintaining 853 mA h g^{-1} after 150 cycles. In addition, the SiO_x/C manifests a specific capacity of 689 mA h g^{-1} at 500 mA g^{-1} and a capacity retention of 91.0% after 400 cycles. The outstanding electrochemical performances enable robust full-cell operations in pairing with $LiFePO_4$, delivering an energy density of 372 W h kg^{-1}.

2. Experimental section

All the chemical reagents used were purchased from Sinopharm Chemical Reagent Co., Ltd. (Shanghai, China).

2.1. Sample preparation

In this work, SiO_x/C composite microspheres with carbon contents of ~ 20%, 40%, and 60% were designated as SiO_x/C-1, SiO_x/C-2, and SiO_x/C-3 respectively.

For the synthesis of SiO_x/C-1, 1 mL of aqueous ammonia (NH_4OH, 25 wt%) was dispersed in a solution containing 20 mL of deionized water and 10 mL of absolute ethanol. After stirring for 1 h, 1 mL of VTES (vinyltriethoxysilane) was added into the mixture. After a reaction time of 5 h at room temperature, the mixture was transferred into a 100 mL Teflon lined autoclave and hydrothermally treated at 100 °C for 12 h. The organosilica microspheres could be obtained after centrifugation and drying at 70 °C. After annealed at 800 °C (3 °C/min) for 3 h in Ar, the final product, SiO_x/C-1 was obtained.

For the synthesis of SiO_x/C-2, 0.3 mL of aqueous ammonia and 0.1 g of resorcinol was dissolved in a solution containing 20 mL of deionized water and 8 mL of absolute ethanol. After stirring for 1 h, 0.14 mL of formaldehyde was added into the mixture. Subsequently, 1 mL of VTES was added under stirring for 24 h at room temperature. The organosilica-polymer microspheres could be obtained after centrifugation and drying. After annealed at 800 °C (3 °C/ min) for 3 h in Ar, the SiO_x/C-2 was obtained. The synthesis of SiO_x/C-3 is quite similar to that of SiO_x/C-2 except different amounts of ethanol (10 mL), resorcinol (0.3 g), ammonia (1 mL) and formaldehyde (0.42 mL) were used.

2.2. Materials characterization

X-ray diffraction (XRD) measurements were performed on a D8 Discover X-ray diffractometer with a non-monochromated Cu Kα X-ray source. Field emission scanning electron microscopy (FESEM) images were collected with a JEOL-7100F microscope at an acceleration voltage of 10 kV. Transmission electron microscopy (TEM) images were recorded by a JEM-2100F STEM/EDS microscope. Brunauer–Emmett–Teller (BET) surface areas were measured using a Tristar II 3020 instrument. Thermo gravimetric analysis (TGA) was conducted using a STA-449C thermogravimetric apparatus. X-ray photoelectron spectrum (XPS) measurement was performed using a VG Multi Lab 2000 instrument.

2.3. Measurements of electrochemical performances

The SiO_x/C composite (75 wt%), acetylene black (10 wt%), and sodium alginate (15 wt%) were dispersed in water to form a slurry. The slurry was spread onto a Cu foil by a doctor blade method, followed by drying in vacuum at 70 °C for 12 h. The mass loading of the active material was 1.5–2 mg cm^{-2}. 1.0 M lithium hexafluorophosphate ($LiPF_6$) in ethylene carbonate/dimethyl carbonate (50/50, v/v) was used as the electrolyte. The electrochemical performances were characterized by assembling CR2016 coin cells with lithium foil as the counter and reference electrode. Galvanostatic discharge/charge measurements were performed in a potential range of 0.01–3.0 V *vs.* Li^+/Li using a multichannel battery testing system (LAND CT2001A). Cyclic voltammetry (CV) and electrochemical impedance spectroscopy (EIS) measurements were tested with an electrochemical workstations (Autolab PGSTAT 302N and CHI600E).

SiO_x/C-2//$LiPFeO_4$ full cells were also assembled. The weight ratio of cathode to anode was around 4:1, and the weight ratio of $LiPFeO_4$:carbon black:PVDF was 80:10:10 in the cathode. The SiO_x/C-2 nanocomposite was firstly pre-lithiated in half cells and then taken out for full cell assembly. The SiO_x/C//$LiFePO_4$ full cells were charged/discharged galvanostatically at 0.2, 0.5, and 1.0 C (1 C = 170 mA h g^{-1}) in the electrochemical window of 2.2–3.75 V.

3. Results and discussion

The synthesis of SiO_x/C microspheres includes two steps, i.e. the sol-gel synthesis of organosilica/polymer composite microspheres and the subsequent conversion into SiO_x/C microspheres (Fig. 1). The synthesis of the organosilica/polymer composite microspheres is carried out under Stöber reaction condition (water-ethanol-ammonia). Under such condition, vinyltriethoxysilane (VTES) is subjected to hydrolysis and condensation, yielding organosilicates; meanwhile, the resorcinol and formaldehyde polymerize, generating a resorcinol-formaldehyde (RF) polymer. Due to the matching reaction kinetics of the above two reactions as well as the strong hydrogen-bond interactions between the silanol (Si-OH) and phenol hydroxyl groups, the organosilica can co-condense with the RF polymer, forming homogeneous organosilica/polymer composite microspheres. During annealing, both the vinyl groups on organosilica and the RF polymer decompose into amorphous carbon, resulting in the formation of homogeneously distributed SiO_x-carbon composite (SiO_x/C) microspheres.

The three SiO_x/C samples show almost identical XRD patterns (Fig. S1). Only a number of very broad diffraction peaks can be observed, implying the amorphous feature of both SiO_x and carbon. According to literatures, the broad peak at ~ 23° can be ascribed to amorphous SiO_x [24], while the wide peak located at ~ 43° can be attributed to amorphous carbon [19,21].

Fig. 2a–f shows the morphology of the obtained SiO_x/C composites. All the samples exhibit regular spherical geometry with good monodispersity. The average diameters of SiO_x/C-1, SiO_x/C-2 and SiO_x/C-3 are determined to be ~ 1000, 400 and 300 nm, respectively. The elemental mapping results of a typical sample, SiO_x/C-2, are shown in Fig. 2g–j. It can be observed that the C, Si and O elements distribute homogeneously in the microspheres, resulting from the co-condensation of organosilica and RF frameworks. The key to the co-condensation is the matching polymerization rates of VTES and resorcinol/formaldehyde under Stöber reaction conditions. It should be pointed out that the co-condensation cannot be achieved if the VTES is substituted by tetraethyl orthosilicate (TEOS) or tetrapropyl orthosilicate (TPOS). According to the literatures, the polymerization of TEOS/TPOS always proceeds much faster than that of resorcinol/formaldehyde, leading to the formation of SiO_2@RF core-shell structures rather than homogeneous SiO_2/RF composites [25–28]. The elemental mapping images of SiO_x/C-1 (Fig. S2) and SiO_x/C-3 (Fig. S3) also show the uniform distribution of C, Si and O.

To further confirm the distribution of SiO_x and C in SiO_x/C-1, it was treated with HF (15 wt%) to remove the SiO_x. Because no resorcinol/formaldehyde is introduced in the synthesis of SiO_x/C-1, the remaining carbon (Fig. S4) is derived from the vinyl group in VTES. The remaining carbon well inherits the micro-spherical morphology of SiO_x/C-1, suggesting that SiO_x species are uniformly dispersed in the carbon matrix. The SiO_x/C-2 and SiO_x/C-3 are obtained through the

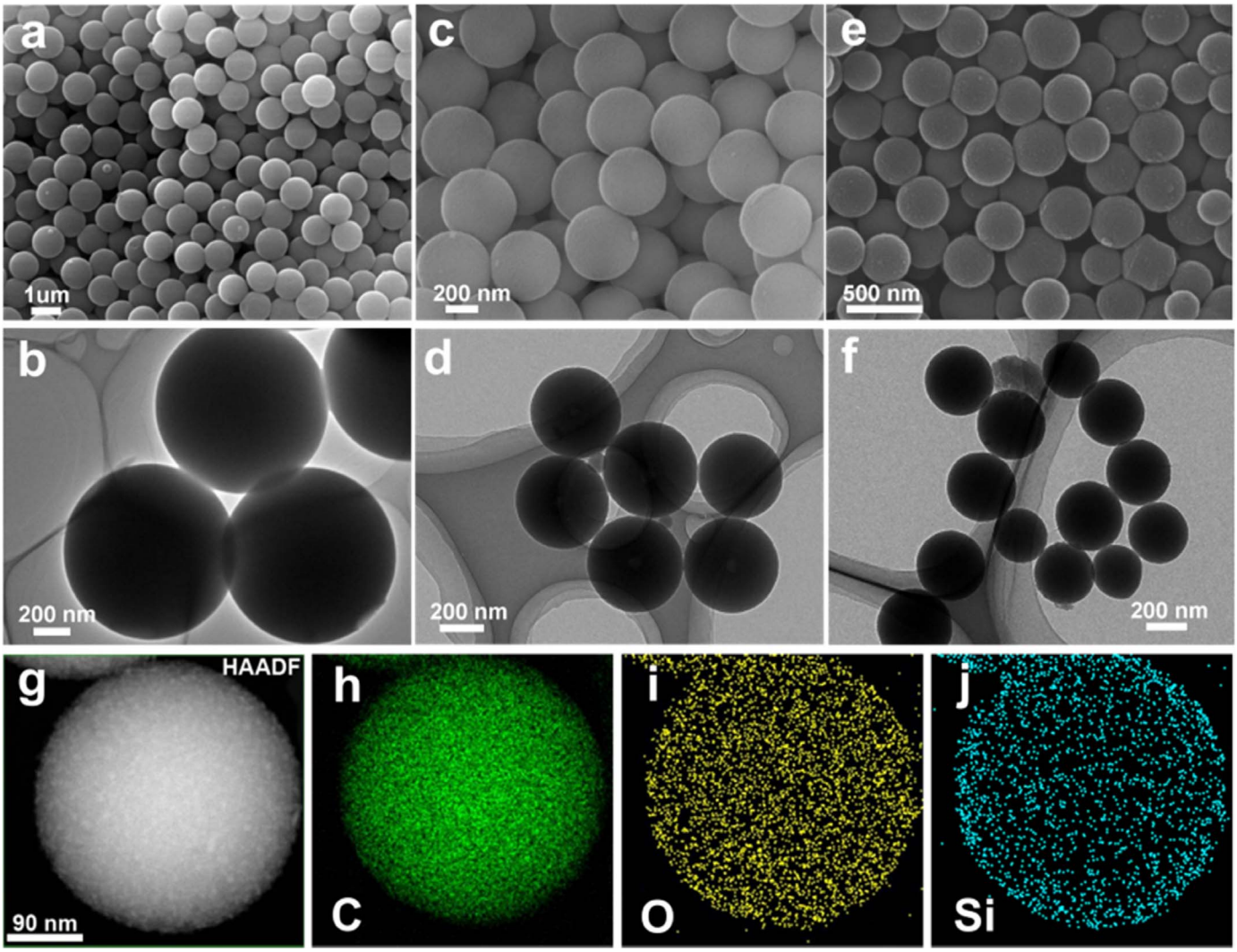

Fig. 2. SEM and TEM images of SiO_x/C-1 (a, b), SiO_x/C-2 (c, d), SiO_x/C-3 (e, f), HAADF-STEM (g) and EDS elemental mapping images (h–j) of SiO_x/C-2.

co-condensation of VTES and resorcinol/formaldehyde, so the carbon is derived from both RF polymer and vinyl groups. Treating the organosilica/RF composite microspheres with HF can remove the organosilica while leaving the RF polymer. Annealing the remaining RF polymer in Ar yields carbon spheres (Figs. S5 and S6) with similar morphology and size to those of SiO_x/C-2 and SiO_x/C-3, demonstrating the even distribution of organosilica in RF framework (co-condensation). Etching the SiO_x species from SiO_x/C-2 yields a microporous carbon (Fig. S7), suggesting the SiO_x species mainly exists as ultrafine nano-domains (< 2 nm). Given the existence of Si–C bond in VTES, the homogeneous distribution of SiO_x and carbon at nanoscale is not surprising.

The BET specific surface area and total pore volume of the SiO_x/C are investigated by nitrogen sorption (Fig. S8). All the SiO_x/C samples exhibit small surface areas (SiO_x/C-1: 2.8 $m^2 g^{-1}$, SiO_x/C-2: 15.4 $m^2 g^{-1}$, SiO_x/C-3: 37.3 $m^2 g^{-1}$) and low pore volumes (SiO_x/C-1: 0.005 $cm^3 g^{-1}$, SiO_x/C-2: 0.009 $cm^3 g^{-1}$, SiO_x/C-3: 0.023 $cm^3 g^{-1}$), indicating their nonporous feature. Such a dense microspherical structure is beneficial for achieving high tap density and thus high volumetric energy density in lithium storage.

Fig. 3a shows the TGA results of the three SiO_x/C composite samples. The carbon contents of SiO_x/C-1, SiO_x/C-2 and SiO_x/C-3 are calculated to be 21.06%, 39.75% and 59.38% respectively. Considering the SiO_x species can be oxidized to SiO_2 during the combustion of carbon, the actual carbon contents of the samples should be slightly higher than the values determined from TGA. The XPS survey spectrum of the sample SiO_x/C-2 (Fig. 3b) confirms that the composite is composed of Si, C, and O. The C1s core level spectrum can be deconvoluted into three components: C in C–C bonds at 284.6 eV, C in C–O bonds at 285.9 eV and C in C=O bonds at 288.9 eV [29]. The Si2p core level spectrum can be fitted into three components, which are attributed to Si^{4+}, Si^{3+}, Si^{2+} respectively [30]. From the high-resolution Si2p spectrum of SiO_x/C-2, the Si^{4+}: Si^{3+}: Si^{2+} ratio is determined to be 35.05%:56.83%:8.12%, and the average valence state of Si is estimated to be ~ 3.27. This value is close to the theoretical valence state of Si (3.0) assuming most of the Si–C bonds in VTES are broken during carbonization [31]. As for SiO_x/C-1 and SiO_x/C-3, both samples show Si average valence states (3.15–3.16) and oxygen contents (x = 1.58) close to those of SiO_x/C-2 (Fig. S9, Table S1).

Fig. S10 displays the initial three cyclic voltammetry (CV) curves of the SiO_x/C-2 composite at a scanning rate of 0.1 mV s^{-1}. Several reactions would happen during the first cathodic process, such as the formation of SEI film, the conversion of SiO_x to lithium silicates, Si, and Li_2O ($SiO_x + 2x\ Li^+ + 2x\ e^- \rightarrow x\ Li_2O + Si$; $SiO_x + x\ Li^+ + x\ e^- \rightarrow 0.25x\ Li_4SiO_4 + (1 - 0.25x)\ Si$, $SiO_x + 0.4x\ Li^+ + 0.4x\ e^- \rightarrow 0.2x\ Li_2Si_2O_5 + (1 - 0.4x)\ Si$), as well as the alloying of Si to Li_xSi ($Si + x\ Li^+ + x\ e^- \leftrightarrow Li_xSi$) [32,33]. The broad cathodic peak located at around 0.32 V in the second and third cycles is due to the formation of Li_xSi alloy, while the anodic peak at 0.42 V is corresponding to the transformation of Li_xSi alloy into Si. The second and third CV curves overlap well, demonstrating the reversible alloying/de-alloying reaction between the *in-situ* generated Si and Li_xSi ($Si + x\ Li^+ + x\ e^- \leftrightarrow Li_xSi$).

Fig. 4a shows the selected discharge-charge curves of SiO_x/C-2 over a potential window of 0.01–3 V at a current density of 100 mA g^{-1}. The initial discharge and charge capacities are 1460 and 965 mA h g^{-1}, respectively. The initial coulombic efficiency is 66.1%. The relatively large irreversible capacity (495 mA h g^{-1}) during the first cycle is due to the formation of SEI film, lithium silicates, and Li_2O [34–36]. From the 2nd to the 150th cycle, the discharge capacity decreases slightly from 999 to 854 mA h g^{-1}, corresponding to a capacity retention of 85.5%. Fig. 4b presents the cyclic performances of SiO_x/C microspheres at a current density of 100 mA g^{-1}. The initial discharge capacity of SiO_x/C-1 reaches 1500 mA h g^{-1}. However, the capacity fades continuously; a value of only 642 mA h g^{-1} remains after 150 cycles, corresponding to a retention of 50.8% against the 2nd cycle. The SiO_x/C-3 delivers a stable discharge capacity of about 625 mA h g^{-1} with negligible tendency of degradation. Several trends can be observed from Fig. 4c and Table 1: (1) the initial coulombic efficiency (CE_{int}) decreases with the increase of carbon content; the SiO_x/C-1 with a lowest carbon content of 21.06% has a highest CE_{int} of 72.4%. This trend suggests the amorphous carbon matrix contributes an important share to the initial irreversible

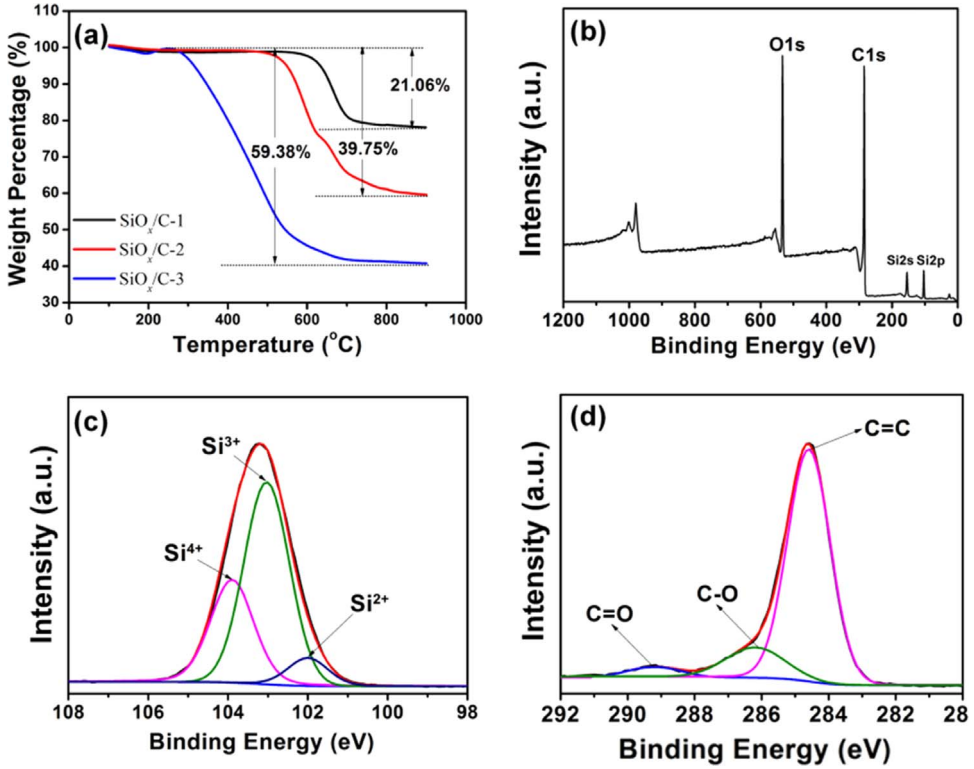

Fig. 3. TGA curves of SiO_x/C microspheres (a), XPS survey spectrum of SiO_x/C-2 (b), high-resolution Si 2p spectrum (c) and high-resolution C1s spectrum (d) of SiO_x/C-2.

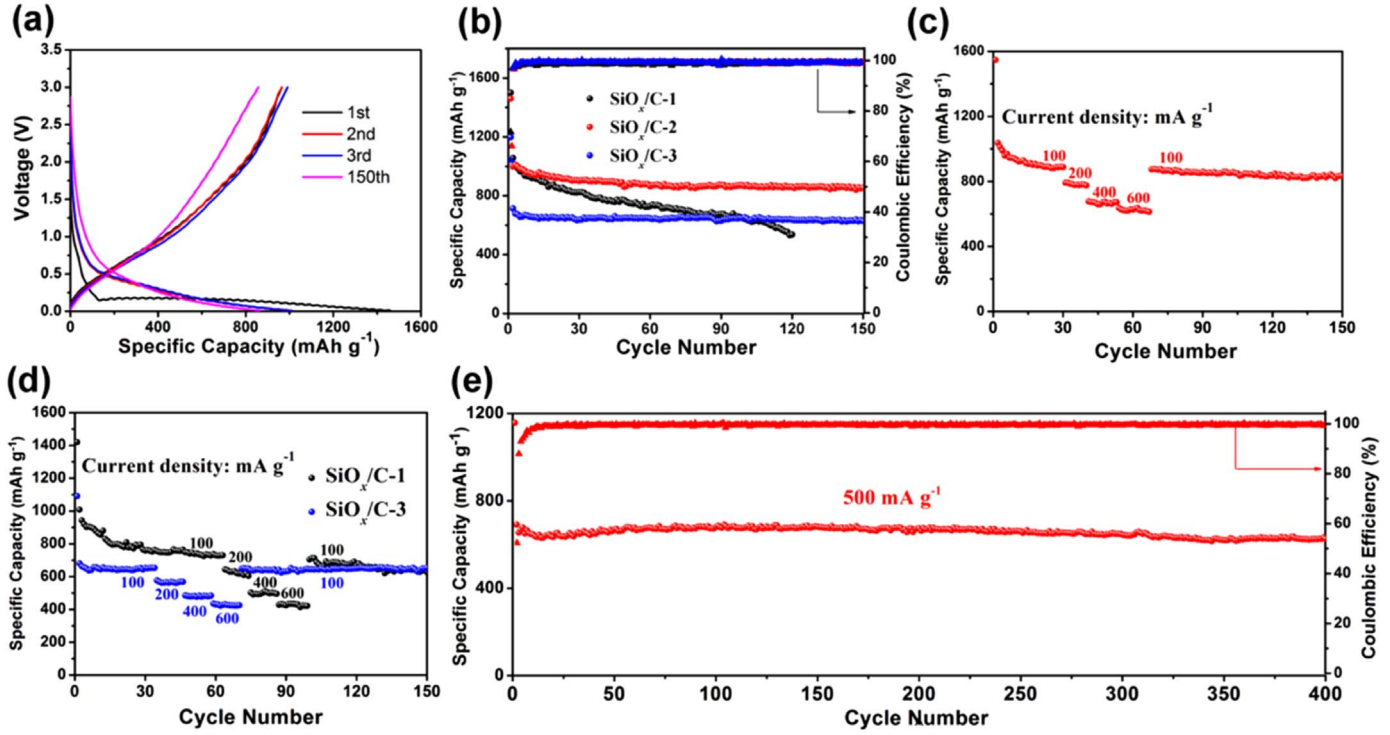

Fig. 4. Discharge-charge profiles of SiO_x/C-2 at a current density of 100 mA g^{-1} (a); cycling performance and coulombic efficiency of SiO_x/C at 100 mA g^{-1} (b); rate capability of SiO_x/C-2 (c); rate capability of SiO_x/C-1 and SiO_x/C-3 (d); long cycling stability and coulombic efficiency of the SiO_x/C-2 at 500 mA g^{-1} for 400 cycles (e).

Table 1
Electrochemical performances of SiO_x/C-1, SiO_x/C-2 and SiO_x/C-3.

Sample	1st discharge capacity	1st coulombic efficiency	Reversible capacity	Capacity retention	Carbon content
SiO_x/C-1	1500	72.4%	1056	50.8%	21.06%
SiO_x/C-2	1460	66.1%	999	85.5%	39.75%
SiO_x/C-3	1197	60.5%	713	88.1%	59.38%

capacity. Similar trend can be observed in the pomegranate-like Si/C nanocomposite and it is caused by the high density of Li trapping sites in amorphous carbon [37]. (2) The reversible capacity (C_{rev}) also decreases with increasing carbon content due to the high theoretical capacity of SiO_x. (3) The capacity retention increases significantly with the carbon content, which can be attributed to the volume change buffering ability of carbon. (4) The SiO_x/C-2 with a moderate carbon content of ~ 39.75% shows the best performance trade-off among CE_{int}, C_{rev} and capacity retention.

The rate performances of SiO_x/C are shown in Fig. 4c and d. With the gradual increase of current density from 100 to 600 mA g^{-1}, the SiO_x/C-2 exhibits a stable discharge capacity at each current density. A stable discharge capacity of ~ 620 mA h g^{-1} can be achieved at 600 mA g^{-1}. When the current density is switched back to 100 mA g^{-1}, the capacity can be recovered to the original value. Due to the higher content of carbon and thus better electronic conductivity, the SiO_x/C-3 manifests much better rate performance than SiO_x/C-1 (Fig. 4e). The SiO_x/C-2 also exhibits outstanding long-cycling performance, At a current density of 500 mA g^{-1}, the SiO_x/C-2 demonstrates a specific capacity of 689 mA h g^{-1} after 400 cycles, corresponding to 91.0% of the 2nd capacity (Fig. 4e). EIS measurements were performed in a frequency range of 100 to 0.01 Hz to explore the interfacial impedance of SiO_x/C with different carbon content (Fig. S11). The sample with higher carbon content shows lower charge-transfer resistance, demonstrating the role of carbon in improving the electrical conductivity.

To evaluate the possibility for practical applications in LIBs, the SiO_x/C-2 was assembled into full cells by pairing with a commercial cathode material, $LiFePO_4$. For anode materials with a low coulombic efficiency, an excess amount of cathode materials are required to compensate the irreversible capacity loss of the first cycle. To make full use of the $LiFePO_4$ cathode material in the full cells, the SiO_x/C-2 was pre-lithiated in a half cell for half a cycle and then took out for full cell assembly. Based on the mass of $LiFePO_4$, the SiO_x/C-2//$LiFePO_4$ full cell delivers specific capacities of 145 and 130 mA h g^{-1} at 0.2 and 1.0 C (Fig. 5a), which are quite close to the capacities of $LiFePO_4$ in half cells (Fig. S12). The corresponding charge/discharge profiles (Fig. 5a inset) exhibit a typical discharge plateaus between 2.8–3.3 V. The cycling performance of the SiO_x/C-2//$LiFePO_4$ full cell is shown in Fig. 5b. The full cell exhibits a reversible capacity of 147 mA h g^{-1} at 0.2 C and maintained at 130 mA h g^{-1} after 100 cycles with a capacity retention ratio of 88.4%. Taking an average voltage value of 3.1 V and an cathode/anode weight ratio of 4:1, the full cell is able to deliver an energy density of 372 W h kg^{-1}, and this value can be further enhanced by optimizing the cathode/anode weight ratio.

The structural integrity is an important parameter for anode materials, especially for high-capacity anode materials suffered from large volume variation. Without proper structural design, such materials would pulverize after repeated discharge-charge processes. For the SiO_x/C samples reported here, their micro-spherical morphology can be well preserved after 150 deep discharge-charge cycles at 100 mA g^{-1} (Fig. 6), demonstrating their excellent structural stability. After 150 cycles, both SiO_x/C-2 and SiO_x/C-3 show a clear and smooth surface after cycling (Fig. 6c and d), suggesting the formation of uniform thin SEI layers on their surface. In contrast, the sample SiO_x/C-1 shows a vague and rough surface (Fig. 6a and b), indicating that the sample is buried under thicker SEI layers. This is reasonable because the SiO_x/C-1 with the lowest carbon content has the largest volume change; the repetitive volume expansion and contraction causes the repeated rupture and formation of SEI layers, resulting the build-up of SEI.

The high reversible capacity and excellent cyclability of SiO_x/C can be attributed to its unique structural features. In the constructed SiO_x/C

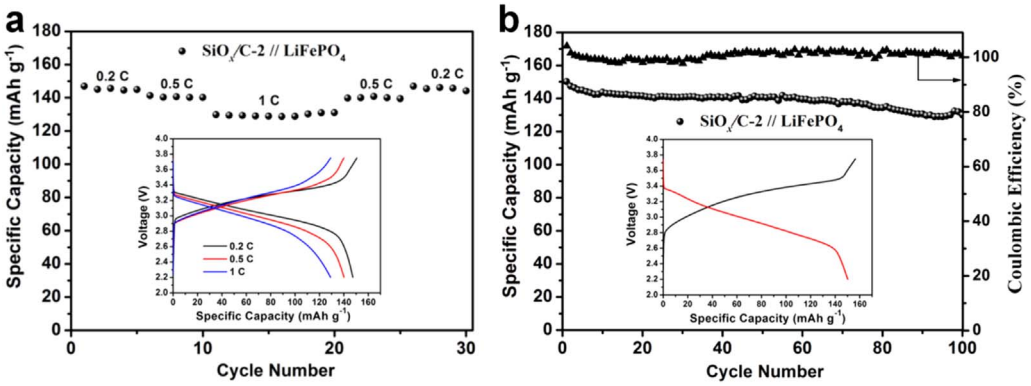

Fig. 5. Rate performance of SiO_x/C-2//$LiFeO_4$ full cell at different C rates (from 0.2 to 1 C) with the corresponding charge/discharge profiles showing in the inset (a); cycling performance of SiO_x/C-2//$LiFeO_4$ full cell at 0.2 C for 100 cycles with the initial charge/discharge profiles showing in the inset (b). The capacity is calculated based on the mass of $LiFePO_4$.

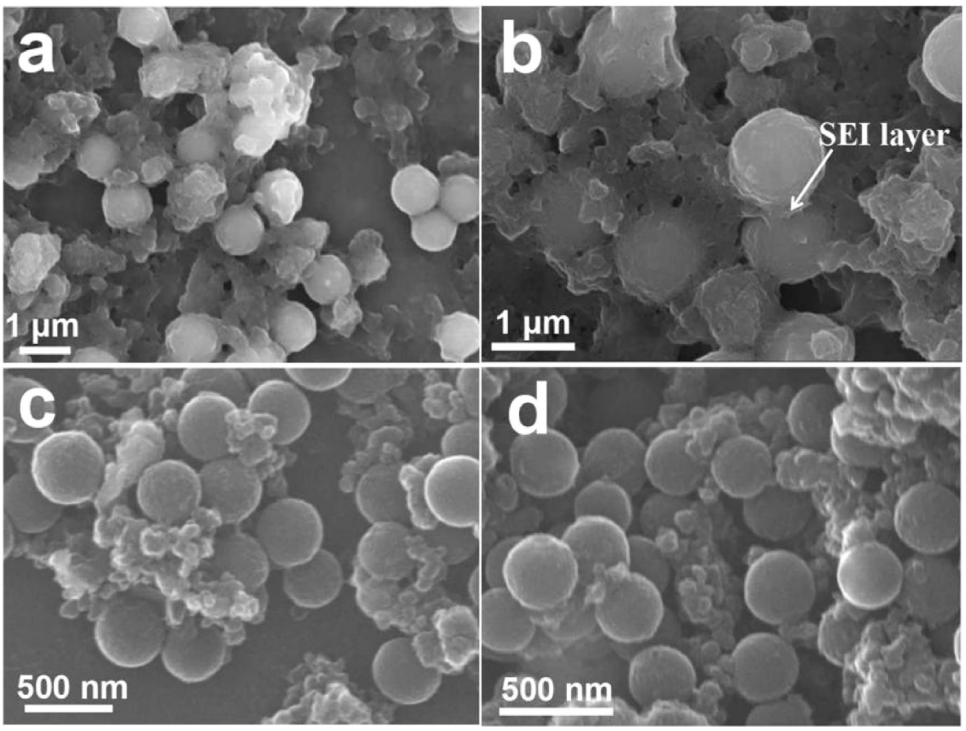

Fig. 6. SEM images of SiO_x/C-1 (a,b), SiO_x/C-2(c), SiO_x/C-3(d) after 150 cycles.

composites, the SiO_x species mainly exists as isolated and ultrafine nano-domains (< 2 nm), evenly distributed in an amorphous carbon matrix. The ultrafine SiO_x is highly active towards lithium and acts as the primary active material, contributing a high capacity to the composites. Meanwhile, the amorphous carbon matrix serves multiple purposes: (I) The amorphous carbon functions as the secondary active component, contributing a certain capacity to the SiO_x/C composite. (II) The amorphous carbon matrix acts as a continuous electron highway, wiring the whole SiO_x/C composite. (III) The amorphous carbon matrix effectively buffers the large volume change, inhibits the aggregation, and prevents the pulverization of SiO_x, resulting in excellent cycling stability. The rate performance of the SiO_x/C composites is not comparable to state-of-the-art anode materials at present, which might be related to their non-porous characteristic. Further improvement of the rate capability is in progress by creating mesopores in the SiO_x/C composites, aiming to boost the sluggish solid-state Li^+ diffusion. The initial Coulombic efficiency of SiO_x based anode materials is generally low, and it might be further enhanced by decreasing O content of SiO_x, improving the graphitization degree of carbon and employing pre-lithiation [38].

4. Conclusion

In summary, monodisperse SiO_x/C composite microspheres with tunable size (300–1000 nm) and well-controlled carbon content (20–60 wt%) have been fabricated via a facile sol-gel co-condensation process using VTES and resorcinol/formaldehyde as precursors. With the homogeneous dispersion of SiO_x ultrafine nano-domains in amorphous carbon matrix, the obtained SiO_x/C composite microspheres manifest high specific capacity (999 mA h g^{-1}), excellent cycling stability (85.5% capacity retention after 150 cycles), and outstanding structural integrity. The SiO_x/C-2//$LiFePO_4$ full cell demonstrated an energy density of 372 W h kg^{-1} with good cycling performance, demonstrating the great potential of SiO_x/C-2 in next-generation LIBs. This work sheds light on the rational design of cost-effective and high-performance SiO_x based anode materials for LIBs.

Acknowledgements

This work was supported by the National Natural Science Fund for Distinguished Young Scholars (51425204), National Key Research and

Development Program of China (2016YFA0202603), National Basic Research Program of China (2013CB934103), Programme of Introducing Talents of Discipline to Universities (B17034), National Natural Science Foundation of China (51521001, 21673171, 51502226), National Fundamental Research Funds for the Central Universities (WUT: 2016III001, 2016III002, 2017III009, 2017III008).

Appendix A. Supplementary material

Supplementary data associated with this article can be found in the online version at doi:10.1016/j.ensm.2018.01.004.

References

[1] M.N. Obrovac, V.L. Chevrier, Chem. Rev. 114 (2014) 11444–11502.
[2] M. Armand, J.M. Tarascon, Nature 451 (2008) 652–657.
[3] J.B. Goodenough, K.S. Park, J. Am. Chem. Soc. 135 (2013) 1167–1176.
[4] B. Dunn, H. Kamath, J.M. Tarascon, Science 334 (2011) 928–935.
[5] Y. Sun, N. Liu, Y. Cui, Nat. Energy 1 (2016) 16071.
[6] H. Kim, M. Seo, M.H. Park, J. Cho, Angew. Chem. Int. Ed. 49 (2010) 2146–2149.
[7] M.H. Park, M.G. Kim, J. Joo, K. Kim, J. Kim, S. Ahn, Y. Cui, J. Cho, Nano Lett. 9 (2009) 3844–3847.
[8] C. Chan, H. Peng, G. Liu, K. McIlwrath, X. Zhang, R.A. Huggins, Y. Cui, Nat. Nanotechnol. 3 (2008) 31–35.
[9] S. Lee, J. Choi, Y. Cui, Nano Lett. 11 (2011) 3034–3039.
[10] D. Lin, Z. Lu, P. Hsu, H. Lee, N. Liu, J. Zhao, Y. Cui, Energy Environ. Sci. 8 (2015) 2371–2376.
[11] Q. Xu, J. Li, J. Sun, Y. Yin, L. Wan, Y. Guo, Adv. Energy. Mater. 7 (2017) 3.
[12] N. Liu, H. Wu, M. McDowell, Y. Yao, C. Wang, Y. Cui, Nano Lett. 12 (2012) 3315–3321.
[13] B. Gao, S. Sinha, L. Fleming, O. Zhou, Adv. Mater. 13 (2001) 816–819.
[14] Y. Yao, J. Zhang, L. Xue, T. Huang, A. Yu, J. Power Sources 196 (2011) 10240–10243.
[15] N. Yan, F. Wang, H. Zhong, Y. Li, Y. Wang, L. Hu, Q. Chen, Sci. Rep. 3 (2013) 1568–1574.
[16] W. Chang, C. Park, J. Kim, Y. Kim, G. Jeong, H.J. Sohn, Energy Environ. Sci. 5 (2012) 6895–6899.
[17] A. Guerfi, P. Charest, M. Dontigny, J. Trottier, M. Lagace, P. Hovington, A. Vijh, K. Zaghib, J. Power Sources 196 (2011) 5667–5673.
[18] S. Hwang, W. Yoon, J. Electrochem. Soc. 161 (2014) A1753–A1758.
[19] J. Cui, Y. Cui, S. Li, H. Sun, Z. Wen, J. Sun, ACS Appl. Mater. Interfaces 8 (2016) 30239–30247.
[20] W. Wu, J. Shi, Y. Liang, F. Liu, Y. Peng, H. Yang, Phys. Chem. Chem. Phys. 17 (2015) 13451–13456.
[21] P. Lv, H. Zhao, C. Gao, Z. Du, J. Wang, X. Liu, J. Power Sources 274 (2015) 542–550.
[22] M. Li, Y. Zeng, Y. Ren, C. Zeng, J. Gu, X. Feng, H. He, J. Power Sources 288 (2015) 53.
[23] Y. Ren, M. Li, J. Power Sources 306 (2016) 459–466.
[24] X. Liu, M. Zheng, K. Xie, J. Liu, Electrochim. Acta. 59 (2012) 304–309.
[25] H. Zhang, M. Yu, H. Song, O. Noonan, J. Zhang, Y. Yang, C. Yu, Chem. Mater. 27 (2015) 6297–6304.
[26] A.B. Fuertes, P. Valle-Vigón, M. Sevilla, Chem. Commun. 48 (2012) 6124–6126.
[27] H. Zhang, O. Noonan, X. Huang, Y. Yang, C. Xu, L. Zhou, C. Yu, ACS Nano 10 (2016) 4579–4586.
[28] Z.A. Qiao, B. Guo, A.J. Binder, J. Chen, G.M. Veith, S. Dai, Nano Lett. 13 (2012) 207–212.
[29] J. Wang, H. Liu, J. Diao, X. Gu, H. Wang, J. Rong, B. Zong, D. Su, J. Mater. Chem. A 3 (2015) 2305–2313.
[30] C. Guo, D. Wang, T. Liu, J. Zhu, X. Lang, J. Mater. Chem. A 2 (2014) 3521–3527.
[31] S. Widgeon, G. Mera, Y. Gao, E. Stoyanov, S. Sen, A. Navrotsky, R. Riedel, Chem. Mater. 24 (2012) 1181–1191.
[32] B. Guo, J. Shu, Z. Wang, H. Yang, L. Shi, Y. Liu, L. Chen, Electrochem. Commun. 10 (2008) 1876–1878.
[33] N. Yan, F. Wang, H. Zhong, Y. Li, Y. Wang, L. Hu, Q.W. Chen, Sci. Rep. 3 (2013) 6.
[34] X. Yang, H. Huang, Z. Li, M. Zhong, G. Zhang, D. Wu, Carbon 77 (2014) 275–280.
[35] H. Zhong, H. Zhan, Y. Zhou, J. Power Sources 262 (2014) 10–14.
[36] P. Hovington, M. Dontigny, A. Guerfi, J. Trottier, M. Lagace, A. Mauger, C.M. Julien, K. Zaghib, J. Power Sources 248 (2014) 457–464.
[37] N. Liu, Z. Lu, J. Zhao, M.T. McDowell, H.W. Lee, W. Zhao, Y. Cui, Nat. Nanotechnol. 9 (2014) 187–192.
[38] H.J. Kim, S. Choi, S.J. Lee, M.W. Seo, J.G. Lee, E. Deniz, Y.J. Lee, E.K. Kim, J.W. Choi, Nano Lett. 16 (2015) 282–288.